PAPER

An enhanced Lamb wave virtual time reversal technique for damage detection with transducer transfer function compensation

IOP Publishing Smart Materials and Structures
Smart Mater. Struct. **28** (2019) 085017 (16pp) https://doi.org/10.1088/1361-665X/ab1fc8

An enhanced Lamb wave virtual time reversal technique for damage detection with transducer transfer function compensation

Junzhen Wang and Yanfeng Shen

University of Michigan-Shanghai Jiao Tong University Joint Institute, Shanghai Jiao Tong University, Shanghai, 200240, People's Republic of China

E-mail: yanfeng.shen@sjtu.edu.cn

Received 6 February 2019, revised 11 April 2019
Accepted for publication 7 May 2019
Published 1 July 2019

Abstract

The Lamb wave time reversal method has widely been investigated as a baseline-free damage detection technique for structural health monitoring. Due to the mode tuning effects from the transducer-wave interactions, even for a pristine wave path, the reconstructed signal waveform may differ much from the original excitation waveform. Consequently, it becomes difficult to distinguish the differences between undamaged and damaged wave paths. This article presents an enhanced Lamb wave virtual time reversal (VTR) algorithm with transducer transfer function compensation to eliminate the transducer influence for dispersive, multimodal Lamb waves. This VTR procedure builds upon a complete 2D analytical model for Lamb wave generation, propagation, and reception. The analytical solution shows that, with the transducer transfer function compensation, a perfect reconstruction of the original excitation waveform can be achieved for both symmetric and antisymmetric Lamb modes. In addition, finite element modeling and experimental validations are further performed to verify the enhanced time reversal procedure. Finally, a time reversal tomography experiment is conducted with a piezoelectric transducer array for structural damage imaging. The enhanced VTR method can achieve more accurate and robust damage imaging results. The paper finishes with discussion, concluding remarks, and suggestions for future work.

Keywords: time reversal, structural health monitoring, non-destructive evaluation, damage detection, Lamb waves, ultrasonics, transducer transfer function

(Some figures may appear in colour only in the online journal)

1. Introduction

Lamb waves have been widely investigated as a powerful tool for the active sensing of thin-plate structures. They can travel long distances with little energy loss and permit the inspection of large structural areas from a single location [1]. A large family of Lamb wave based structural health monitoring (SHM) methodologies have been proposed, such as the phased array ultrasonic radar, the sparse array pitch-catch damage imaging method, nonlinear ultrasonics, and the time reversal (TR) techniques, etc [2–9].

The concept of TR invariance was first introduced by Fink and his colleagues [10, 11]. Recently, the SHM and non-destructive evaluation (NDE) communities have studied TR methods for damage detection. Wang *et al* combined the TR and synthetic aperture technique for damage imaging [8]. Baseline-free imaging algorithms have been developed via the backward propagation of the scattered waves [12, 13]. Park *et al* interpreted the residual side packages in the reconstructed TR signals induced by multiple Lamb modes and boundary reflections [14]. Jeong *et al* simulated the TR process for the baseline-free imaging of a defect [15]. Based

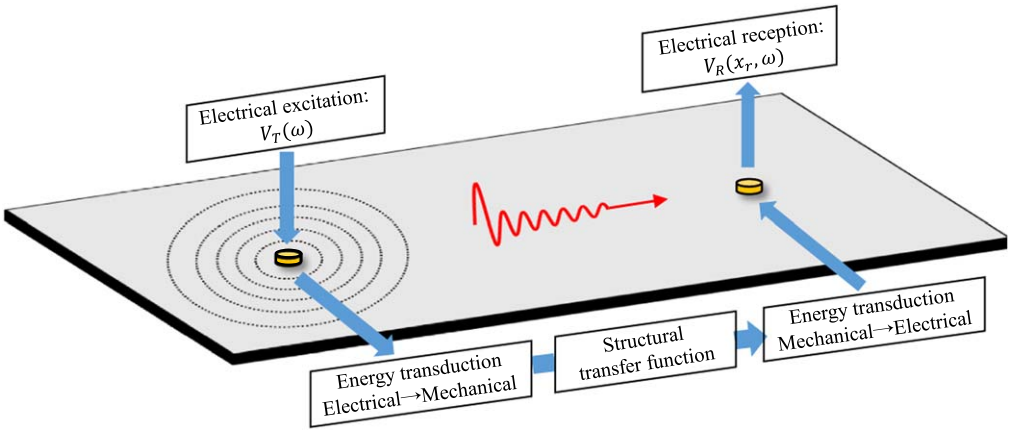

Figure 1. A typical pitch-catch active sensing procedure.

on the decomposition of Lamb wave TR operator, the position of damage zones can be estimated [16]. Poddar *et al* studied different parameters such as the center frequency, pulse frequency band width, and transducer size on the quality of the reconstructed signal [17]. In addition, TR techniques have also been applied on composite materials [9, 18, 19]. Sohn *et al* employed a wavelet transform technique to improve the time reversibility of Lamb waves in composite structures [20]. Agrahari and Kapuria refined the damage indices with extended signal length so as to improve the sensitivity of the TR approach to the structural damage [21]. Watkins and Jha presented a modified time reversal method [22], in which the transmitter would emit the time-reversed signal into the system again, whereas in the conventional TR procedure, the transmitter and the receiver would have to take turns to send ultrasonic waves into the structure. Zeng *et al* adopted the modified Lamb wave TR method with amplitude modulation and achieved improved damage imaging in composite structures [23]. To reduce the practical hardware operations, Liu *et al* proposed a virtual time reversal (VTR) algorithm and inspected delamination with non-contact air-coupled Lamb wave scan method in a carbon fiber-reinforced composite plate [24]. The VTR technique only needs a typical pitch-catch active sensing signal; the TR procedure is replaced by computerized virtual signal operations. Cai *et al* utilized the VTR-based method with damage scattered wave packages to improve the spatial resolution of the diagnostic images [25].

However, it has been noticed that, in the application of TR methods, even for a pristine wave path, the reconstructed waveform may deviate from the original excitation waveform. It is because the tuning effects from the wave-transducer interactions may modify the frequency contents of the sensing signals, causing waveform distortions during the electro-mechanical energy conversion process. Nevertheless, such a seemingly trivial aspect was often overlooked. To the best of the authors' knowledge, the systematic study considering the transducer effects is still very limited. Recently, Kim *et al* explored the VTR technique using non-dispersive, fundamental shear horizontal waves to detect holes in a metallic plate; they demonstrated that transducer transfer function compensation can considerably improve the quality of the diagnostic images [26]. Although the wave generation mechanism of piezoelectric wafer active sensors (PWAS) has been well studied, the transducer transfer function compensation for multimodal, dispersive Lamb waves has been seldom considered for TR techniques [27, 28]. It should be pointed out that Xu and Giurgiutiu have taken advantage of the tuning effect to realize single mode TR process [29]. However, the transducer influence on the multimodal Lamb waves at arbitrary excitation frequencies has not been considered for the improved time-reversibility. Thus, this research effort differs from the previous investigations and facilitates a new approach to enhance the damage evaluation capability of TR techniques.

This paper presents an enhanced Lamb wave VTR technique with transducer transfer function compensation for improved damage detection. This research initiates with the development of a 2D analytical model of the pitch-catch active sensing procedure in order to attain the transducer transfer functions. Subsequently, the enhanced VTR method is illustrated in details by introducing a step-by-step compensation algorithm. The reconstructed signals from analytical solution, FE simulations and experiments are compared before and after the transducer transfer function compensation to demonstrate the improvement of the time-reversibility. Finally, VTR tomography imaging experiments are performed; the comparison between conventional VTR and enhanced VTR algorithm images are given to showcase the improved diagnostic capability of our new approach.

2. 2D analytical model for Lamb wave active sensing

The enhanced VTR algorithm is realized via compensating the transducer transfer function. Thus, an in-depth understanding of the pitch-catch active sensing procedure is of critical importance. Admittedly, the analytical solution has been well studied in several existing literatures [30, 31], yet this section strives to systematically unfold the model to identify the target transfer function expression for compensation in the TR algorithm.

Figure 1 presents a typical pitch-catch procedure. Lamb waves are generated by the transmitter through the inverse piezoelectric effect, converting electrical excitation into the mechanical disturbances. The mechanical oscillations will be guided along the plate structure forming multiple Lamb wave modes traveling with different wave speeds. Finally, the mechanical wave motion will be picked up by the receiver, where the mechanical energy is converted back into the electrical sensing signal.

The detailed derivation of the 2D Lamb wave active sensing solution between two circular PWAS transducers can be found in [32–34]. The relationship between the excitation waveform $V_T(\omega)$ and the sensing waveform $V_R(\omega)$ is given by

$$V_R(\omega) = -\pi i \frac{a\kappa_t(\omega) g_{31} E_s h}{\mu} \left[\sum_{\xi^S} \frac{J_1^2(\xi^S a) N_S(\xi^S)}{D_S'(\xi^S)} H_0^{(1)}(\xi^S x_r) + \sum_{\xi^A} \frac{J_1^2(\xi^A a) N_A(\xi^A)}{D_A'(\xi^A)} H_0^{(1)}(\xi^A x_r) \right] V_T(\omega), \quad (1)$$

where ω is the angular frequency; a represents the radius of the circular piezoelectric transducer; μ denotes the shear modulus of the structure; g_{31} stands for the piezoelectric voltage constant; E_s and h denote the Young's modulus and thickness of the receiver; x_r is the distance between the transmitter and the receiver; J_1 represents the Bessel function of order one, which captures the tuning effect between the transducer and the host structure considering both excitation and reception procedures; $H_0^{(1)}$ stands for the Hankel function of the first kind and order zero, which represents an outward propagating 2D wave field. The rest component functions are defined as

$$\begin{aligned} N_S(\xi) &= \xi\eta_S(\xi^2 + \eta_S^2)\cos\eta_P d \cos\eta_S d \\ N_A(\xi) &= -\xi\eta_S(\xi^2 + \eta_S^2)\sin\eta_P d \sin\eta_S d \\ D_S &= (\xi^2 - \eta_S^2)^2 \cos\eta_P d \sin\eta_S d + 4\xi^2\eta_P\eta_S \sin\eta_P d \cos\eta_S d \\ D_A &= (\xi^2 - \eta_S^2)^2 \sin\eta_P d \cos\eta_S d + 4\xi^2\eta_P\eta_S \cos\eta_P d \sin\eta_S d, \end{aligned} \quad (2)$$

where d denotes half plate thickness; $\frac{N_S(\xi^S)}{D_S'(\xi^S)}$ and $\frac{N_A(\xi^A)}{D_A'(\xi^A)}$ depict the Lamb wave modes of the structure; ξ is the frequency dependent wavenumber calculated from the Rayleigh–Lamb equation [35, 36]:

$$\begin{aligned} &\frac{\tan\eta_S d}{\tan\eta_P d} = \left[\frac{-4\eta_P\eta_S\xi^2}{(\xi^2 - {\eta_S}^2)^2} \right]^{\pm 1} \\ &{\eta_P}^2 = \frac{\omega^2}{c_P^2} - \xi^2; \quad {\eta_S}^2 = \frac{\omega^2}{c_S^2} - \xi^2; \\ &c_P = \sqrt{\frac{\lambda + 2\mu}{\rho}}; \quad c_S = \sqrt{\frac{\mu}{\rho}}, \end{aligned} \quad (3)$$

where $+1$ exponent corresponds to symmetric Lamb wave modes and -1 exponent corresponds to antisymmetric Lamb wave modes. c_P and c_S represent the P-wave speed and S-wave speed; λ is Lame's constant of the structural material; ρ is the material density. The transmitter complex transduction coefficient, $\kappa_t(\omega)$, which converts applied voltage $V_T(\omega)$ into the shear stress, is given by

$$\kappa_t(\omega) = \frac{d_{31}}{s_{11}^E} \frac{r(\omega)}{1 - r(\omega)}, \quad (4)$$

where $r(\omega)$ is the stiffness ratio between the transmitter transducer and the host structure [37]. At a given excitation frequency ω, equation (3) yields a multitude of symmetric (S) and antisymmetric (A) wavenumbers ξ^S, ξ^A which are used in calculating the summations contained in equation (1), rendering two classes of de-coupled wave motions.

Upon careful observation of equation (1), it can be noticed that the excitability function, the tuning function, and the Hankel function are all frequency dependent. They would modify the participation of different frequency components during the active sensing energy transduction procedure. Thus, the transducer transfer functions for symmetric and antisymmetric modes can be identified as

$$G^S(x_r, \omega) = -\pi i \frac{a\kappa_t(\omega) g_{31} E_s h}{\mu} \times \sum_{\xi^S} \frac{{J_1}^2(\xi^S a) N_S(\xi^S)}{D_S'(\xi^S)} H_0^{(1)}(\xi^S x_r) \quad (5)$$

$$G^A(x_r, \omega) = -\pi i \frac{a\kappa_t(\omega) g_{31} E_s h}{\mu} \times \sum_{\xi^A} \frac{{J_1}^2(\xi^A a) N_A(\xi^A)}{D_A'(\xi^A)} H_0^{(1)}(\xi^A x_r). \quad (6)$$

Equations (5) and (6) will be used to compensate the VTR signals. It should be emphasized that the compensation algorithm includes both the piezoelectric transduction and the 2D wave propagation feature inside of the host structure.

3. Enhanced VTR algorithm

This section presents the enhanced VTR algorithm by comparing with the conventional VTR procedure. It should be noted that the existing literatures on VTR generally adopted single wave mode, A0 mode in [23] and SH0 mode in [26]. This study considers the dispersive and multi-modal characteristics of Lamb wave. Both S0 and A0 Lamb wave modes are processed by the proposed VTR algorithm.

Following [23], the essence of the conventional VTR of Lamb waves can be appreciated with

$$V_C(\omega) = V_R^*(\omega) \frac{V_R(\omega)}{V_T(\omega)}, \quad (7)$$

where $V_T(\omega)$ is the excitation waveform applied on the transmitter in the real forward process; $V_R(\omega)$ represents the signal picked up by the receiver in the frequency domain; $V_C(\omega)$ denotes the reconstructed waveform at receiver in the virtual backward process; the superscript * denotes a complex conjugate processing, facilitating the TR operation of a signal in the frequency domain. Figure 2 presents such a

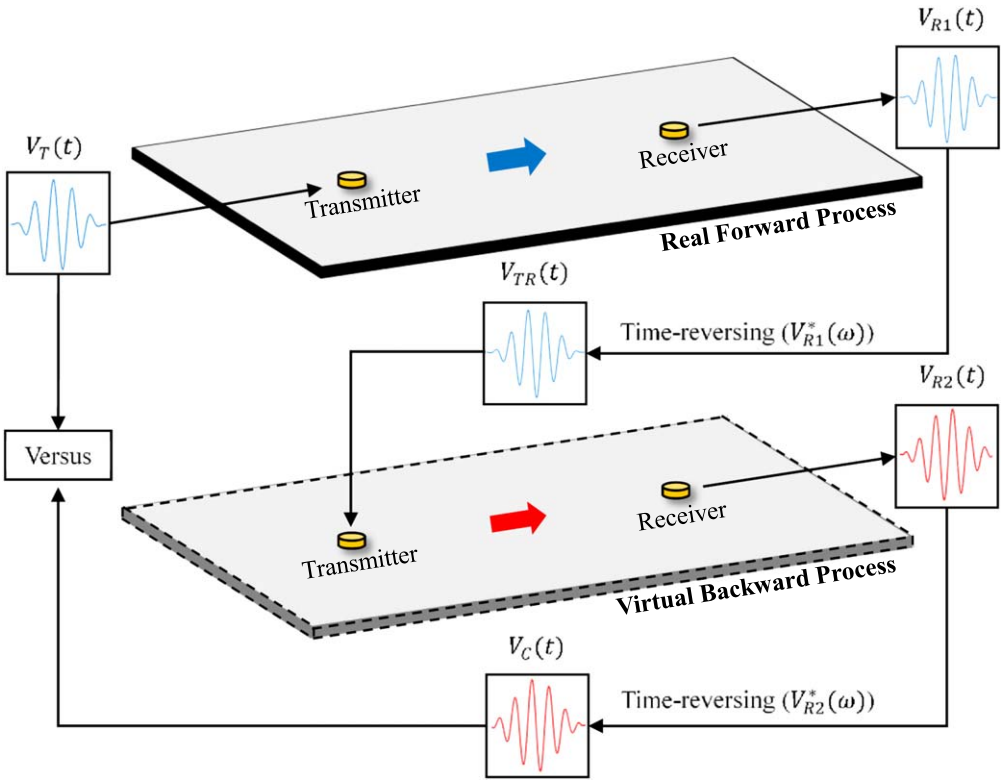

Figure 2. Schematic of the conventional VTR algorithm.

conventional VTR setup. Only one physical pitch-catch procedure is needed, considerably reducing the hardware manipulation by substituting the backward time-reversal pitch-catch procedure by a virtual operation.

The term $\frac{V_R(\omega)}{V_T(\omega)}$ in equation (7) provides the transfer function between the electrical excitation and the sensing signal. Such a transfer function contains both the transducer effect and the structural influence. Then, it operates on the time-reversed sensing signal $V_R^*(\omega)$, achieving the backward transmission procedure. Nevertheless, the transducer influence exists in both the forward and backward transmission procedures, which would modify the frequency contents of the reconstructed signal even if no damage exist along the wave path. The enhanced VTR algorithm strives to remove such frequency modification factors in the signal reconstruction procedure and improve the time reversibility of the Lamb modes.

Figure 3 presents the schematic of the proposed enhanced VTR algorithm. The apparent improvement over the conventional VTR and enhanced VTR algorithm is that the multi-modes and transducer influences are considered. The enhanced VTR algorithm can be achieved in the following steps:

STEP 1: Conduct pitch-catch active sensing by applying electrical excitation $V_T(\omega)$ on the transmitter. The sensing signal $V_{R1}(\omega)$ can be expressed as:

$$V_{R1}(\omega) = G(\omega)D(\omega)V_T(\omega), \tag{8}$$

where $G(\omega)$ is the transducer transfer function, respectively for S0 and A0 modes in equations (5) and (6). $D(\omega)$ represents the damage influence on the sensing signals. For a pristine structure, $D(\omega)$ takes the value of 1 for all the frequencies, imposing a null effect on the sensing signals. Here, the above formulation represents the typical multi-modal Lamb wave generation, propagation, interaction with the damage, and reception.

STEP 2: Single mode wave packages are separated using a smooth window function. The location of the windows are determined according to the group velocities of different Lamb wave modes. In addition, the lengths of windows are set to cover the entire single mode wave package. It should be noticed that such separation of modes can be difficult to achieve in complex practical scenarios. For example, when the wave path is short, the wave packages will overlap with each other, making it challenging for effective mode separation. In this study, the piezoelectric transducers are implemented far away from each other, which would guarantee S0 and A0 modes have been well separated in the temporal and spatial domain when they arrive at the receivers.

STEP 3: Time reverse the S0 and A0 packages respectively by carrying out the complex conjugate operation $V^*_{R1}(\omega)$ in frequency domain. $V_{\mathrm{TR}}(t)$ denotes the time reversed signal for both S0 and A0 modes in time domain.

STEP 4: Re-emit the reversed signal back to the transmitter in the virtual backward process, and obtain the sensing signal from the receiver. The sensing signal $V_{R2}(\omega)$ in the virtual backward process can be expressed as:

$$\begin{aligned} V_{R2}(\omega) &= V^*_{R1}(\omega)G(\omega)D(\omega) \\ &= [G(\omega)D(\omega)V_T(\omega)]^* G(\omega)D(\omega). \end{aligned} \tag{9}$$

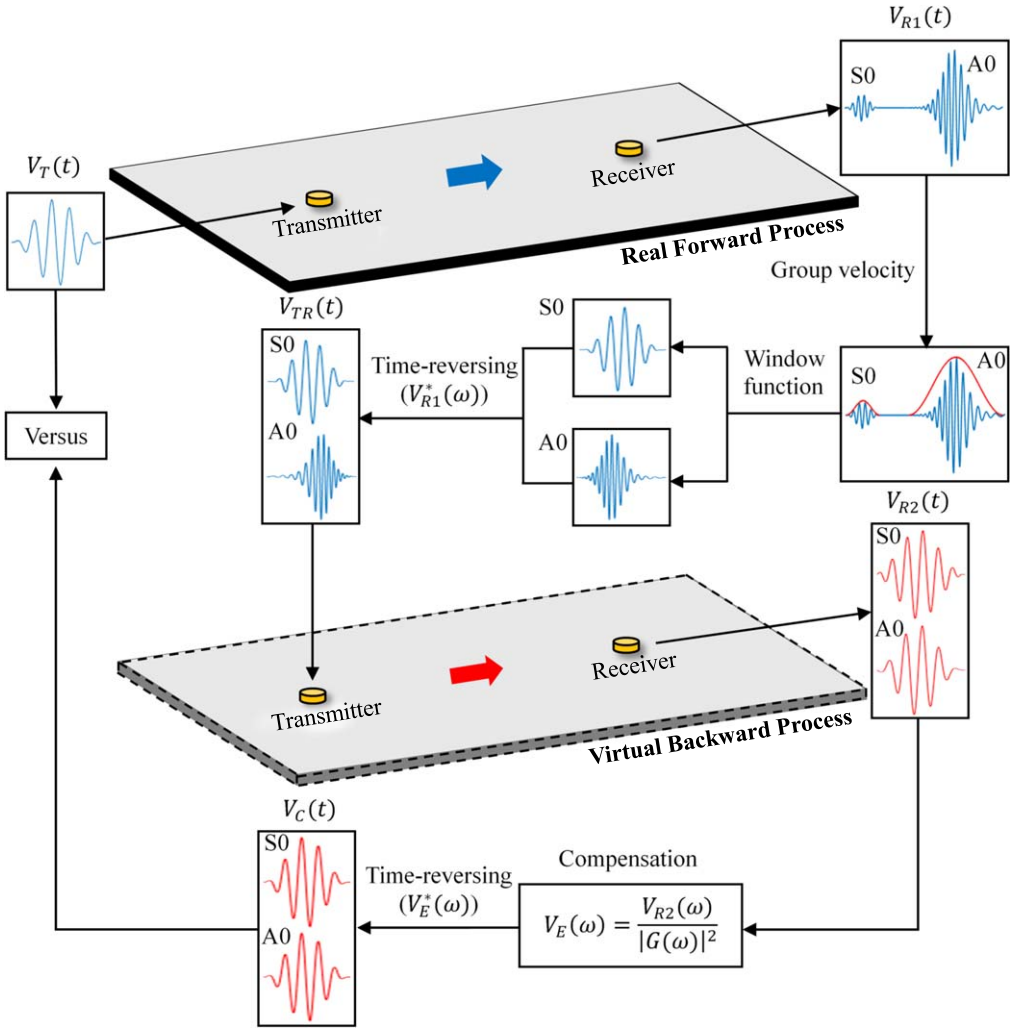

Figure 3. Schematic of the proposed enhanced VTR algorithm.

The complex conjugate properties lead to the simplification of the above formulation as

$$V_{R2}(\omega) = G(\omega)G^*(\omega)D(\omega)D^*(\omega)V_T^*(\omega) = |G(\omega)|^2|D(\omega)|^2V_T^*(\omega). \quad (10)$$

STEP 5: Apply the transducer transfer function compensation algorithm on the virtual backward sensing signal. The compensated signal $V_E(\omega)$ can be expressed as:

$$V_E(\omega) = \frac{V_{R2}(\omega)}{|G(\omega)|^2} = V_T{}^*(\omega)\ |D(\omega)|^2. \quad (11)$$

STEP 6: Time reverse the compensated signal. The reconstructed signal can be expressed as:

$$V_C(\omega) = V_E^*(\omega) = V_T(\omega)\ |D(\omega)|^2. \quad (12)$$

Thus, for the pristine case, where $D(\omega) = 1$, the reconstructed signal in the frequency domain after compensation will trace back to the exact original excitation waveform.

STEP 7: Perform inverse Fourier transform on the frequency domain reconstructed signal $V_C(\omega)$ and obtain the time domain reconstructed waveform

$$V_C(\mathrm{t}) = IFFT[V_C(\omega)]. \quad (13)$$

The time domain reconstructed signal can be compared with the original electrical excitation V_T(t) to draw diagnostic conclusions. Therefore, via the analysis, the following five remarks should be made:

(1) The above formulation clearly demonstrates that two influence sources on the reconstructed waveform inevitably coexist: (a) structural damage, the target factor desired to be extracted from the VTR procedure; (b) transducer dynamics, the adverse system influence desired to be excluded from the VTR signals.

(2) The influence from the transducer dynamics may become dominant and crucial, especially when the damage is incipient and small. Thus, compensating the transducer transfer function in the VTR algorithm reveals its undeniable significance for improving the sensitivity and accuracy of TR SHM/NDE techniques to detect early-stage defects.

(3) It should be noted that the transducer transfer function $G(\omega)$ possesses close-form exact analytical solution given by equations (5) and (6) for PWAS transducers. But the compensation algorithm generally applies by

taking alternative forms for other types of transducers. In addition, if a close-form analytical solution cannot be readily attained, experimental tuning data may serve as another route to obtain the transducer function. The beauty of analytical expressions for transducer transfer functions lies in the fact that they allow the algorithm to maintain a complete virtual computation and alleviate the instrumentation operations.

(4) In this study, the transducer tuning effects are considered for the transfer function compensation procedure. However, many other important factors may also participate in the formulation and influence the Lamb wave propagation signals, such as the temperature effect and loading conditions. This study serves as our initial endeavor for compensating the transducer effects in the TR technique. The temperature and loading effects should be investigated for the TR procedure in a future research effort.

(5) The compensation algorithm could be extended for anisotropic composite structures. But there still exist considerable challenges to be investigated in the future. Due to the anisotropic characteristics of composite structure, the transducer transfer function becomes direction dependent. As a result, the analytical solution of transducer transfer function needs to be evaluated for each propagation direction. Furthermore, the damping effect should also be considered, which would remarkably affect the wave dynamics in the composite structure.

4. Signal reconstruction results

To illustrate the efficacy of our enhanced VTR algorithm with transducer transfer function compensation, the signal reconstruction quality comparison with the conventional VTR is presented in this section.

The difference between the reconstructed signal and the excitation waveform is usually used as a baseline free index for evaluating structural damage. The damage index (DI) or the time reversibility index is widely adopted taking the signal correlation concept [20]

$$\mathrm{DI} = 1 - \frac{\left| \int_{t_0}^{t_1} I(t)V(t)dt \right|}{\sqrt{\int_{t_0}^{t_1} I^2(t)dt \int_{t_0}^{t_1} V^2(t)dt}}, \tag{14}$$

where $I(t)$ represents the input excitation signal; $V(t)$ denotes the final reconstructed signal from VTR procedure; t_0 and t_1 define the time interval over which the signals are compared. For TR signals, they represent the starting and ending time instance of the input tone burst signal.

4.1. Analytical results comparison

The pitch-catch and TR procedure was first investigated using the analytical model developed in sections 2 and 3. A 20 Vpp five-count Hanning window modulated sine tone burst signal centered at 100 kHz was applied on the top electrode of the transmitter. Figure 4 presents the excitation, pitch-catch active sensing signal, as well as their frequency spectra for both the analytical solution and the experimental results. It should be noted that the excitation signal possesses a certain band-width as well as side lobes in frequency domain. The S0 and A0 packages can be clearly identified in the sensing time trace. It should be noted that, in the experimental signal, an electromagnetic (E/M) coupling signal exists before S0 mode. Other than this aspect, the analytical solution agrees very well with the experimental measurement. In addition, the central frequency of these two Lamb wave modes experienced a shift compared with that of the excitation. For the analytical solution, the central frequency of S0 mode shifted upward to 103 kHz, whereas the A0 mode shifted downward to 99 kHz. The experimental A0 mode also shifted to 99 kHz with a remarkable match with the analytical prediction. And the experimental S0 mode shift upward to 106 kHz which is close enough but a little bit higher than the analytical S0 mode prediction. The frequency component shift phenomenon happened due to the transducer tuning effect, which apparently changed the frequency participation of the Lamb wave modes across the generated frequency range. Such effect may become more obvious at other excitation center frequencies, imposing stronger influence on the time reversibility of the Lamb modes.

Figure 5 presents the reconstructed signals before and after the transducer transfer function compensation via the VTR procedure. The reconstructed signal utilizing the conventional VTR algorithm could not match well with the excitation waveform. This is especially true for S0 mode, which means the tuning phenomenon remarkably changes the frequency participation of the S0 mode signal. By comparison, the analytical solution of the enhanced virtual TR algorithm renders a perfect agreement between the reconstructed signal and the excitation waveform for both S0 and A0 modes. Such an improvement stems from the fact that the transducer influence was completely compensated by the enhanced VTR algorithm.

The analytical solution allows the TR procedure to maintain its virtual operation capability, which averts additional hardware intervention. However, the proposed algorithm should guarantee the improved time reversibility for applications in both numerical models and experiments. Such an aspect will be presented in the following two sub-sections.

4.2. Finite element simulation results comparison

The pitch-catch procedure was simulated using FEM as shown in figure 6. Two 7-mm diameter 0.2-mm thick circular piezoelectric transducers are considered ideally bonded on a 1-mm thick aluminum plate. The APC-850 material

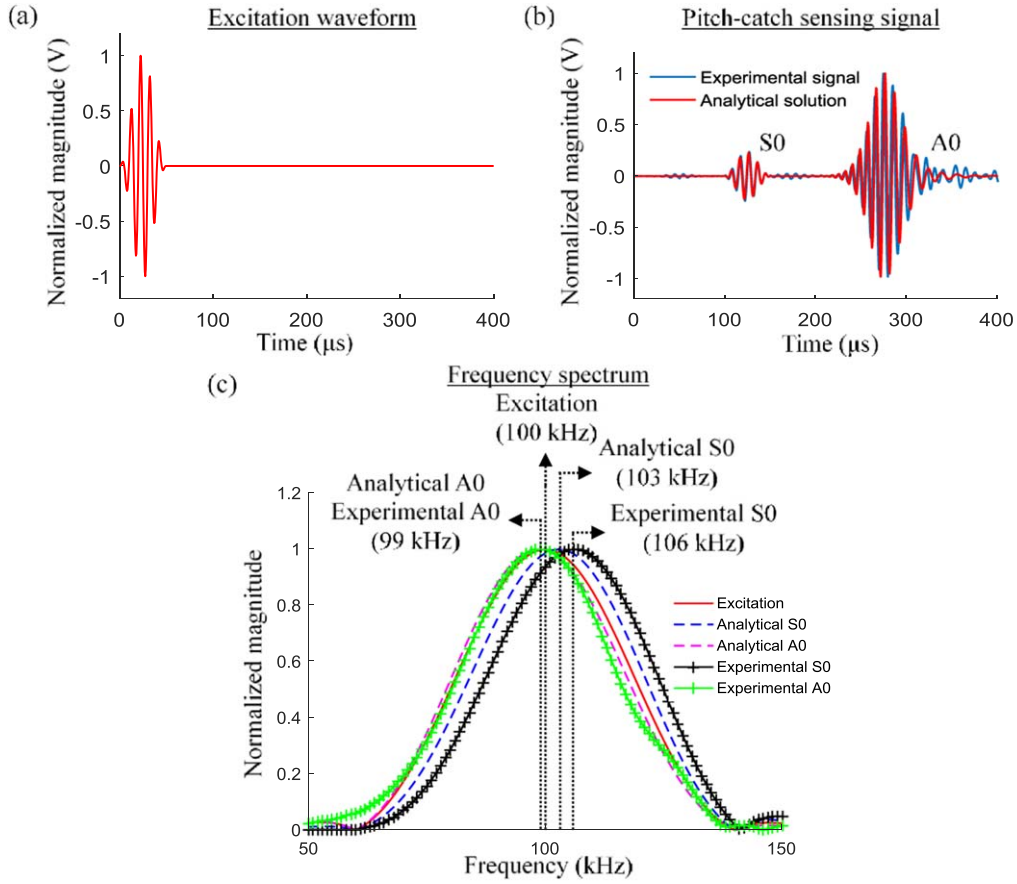

Figure 4. Excitation signal and sensing signal in time domain and frequency domain: (a) excitation signal; (b) sensing signal; (c) frequency contents of S0 and A0 packages as well as the excitation.

properties are assigned to the piezoelectric transducers as follows:

$$[C_p] = \begin{bmatrix} 97 & 49 & 49 & 0 & 0 & 0 \\ 49 & 84 & 49 & 0 & 0 & 0 \\ 49 & 49 & 97 & 0 & 0 & 0 \\ 0 & 0 & 0 & 24 & 0 & 0 \\ 0 & 0 & 0 & 0 & 22 & 0 \\ 0 & 0 & 0 & 0 & 0 & 22 \end{bmatrix} \text{Gpa}, \tag{15}$$

$$[\varepsilon_p] = \begin{bmatrix} 947 & 0 & 0 \\ 0 & 605 & 0 \\ 0 & 0 & 947 \end{bmatrix} \times 10^{-8}\ \text{F m}^{-1}, \tag{16}$$

$$[e_p] = \begin{bmatrix} 0 & 0 & 0 & 12.84 & 0 & 0 \\ -8.02 & 18.31 & -8.02 & 0 & 0 & 0 \\ 0 & 0 & 0 & 0 & 12.84 & 0 \end{bmatrix} \text{C m}^{-2}, \tag{17}$$

where $[C_p]$ is the stiffness matrix $[\varepsilon_p]$, is the dielectric matrix, and $[e_p]$ is the piezoelectric matrix. The density of the piezoelectric material takes the value of $\rho = 7600\ \text{kg m}^{-3}$.

To minimize the computational burden, non-reflective boundaries (NRB) were implemented around the model to eliminate the boundary reflections [38]. SOLID5 coupled filed element in ANSYS was used to simulate the piezoelectric transducers. SOLID45 eight node structural element was adopted to mesh the plate. Absorbing layers with increasing damping were implemented to construct the NRB. The mesh size in this study is 1 mm for in-plane direction and 0.5 mm for thickness direction. The transmitter and receiver transducers were meshed with even smaller elements to accommodate the high stress gradient. The time step was set to 0.5 μs.

Figure 7 presents the FE simulation reconstructed signal before and after the transducer transfer function compensation. The reconstructed S0 mode deviates much from the excitation waveform than A0 mode using the conventional VTR method. However, after the transducer transfer function compensation, the reconstructed signal agrees quite well with the excitation signal. As for the A0 mode, smaller difference before and after compensation can be found, which follows the similar trend as the analytical solution.

4.3. Experimental results comparison

Figure 8 presents the experimental setup for the pitch-catch procedure. The specimen was a pristine 700 mm long, 700 mm wide, and 1 mm thick aluminum plate. The transmitter and receiver transducers were implemented 400 mm away from each other, as the same distance in the analytical and FE models. The procedure of bonding the piezoelectric transducers onto the structure follows a strict procedure to ensure a consistent performance. Such a procedure includes accurate sensor positioning, surface preparation with cleaning chemicals, transducer bonding utilizing special adhesives,

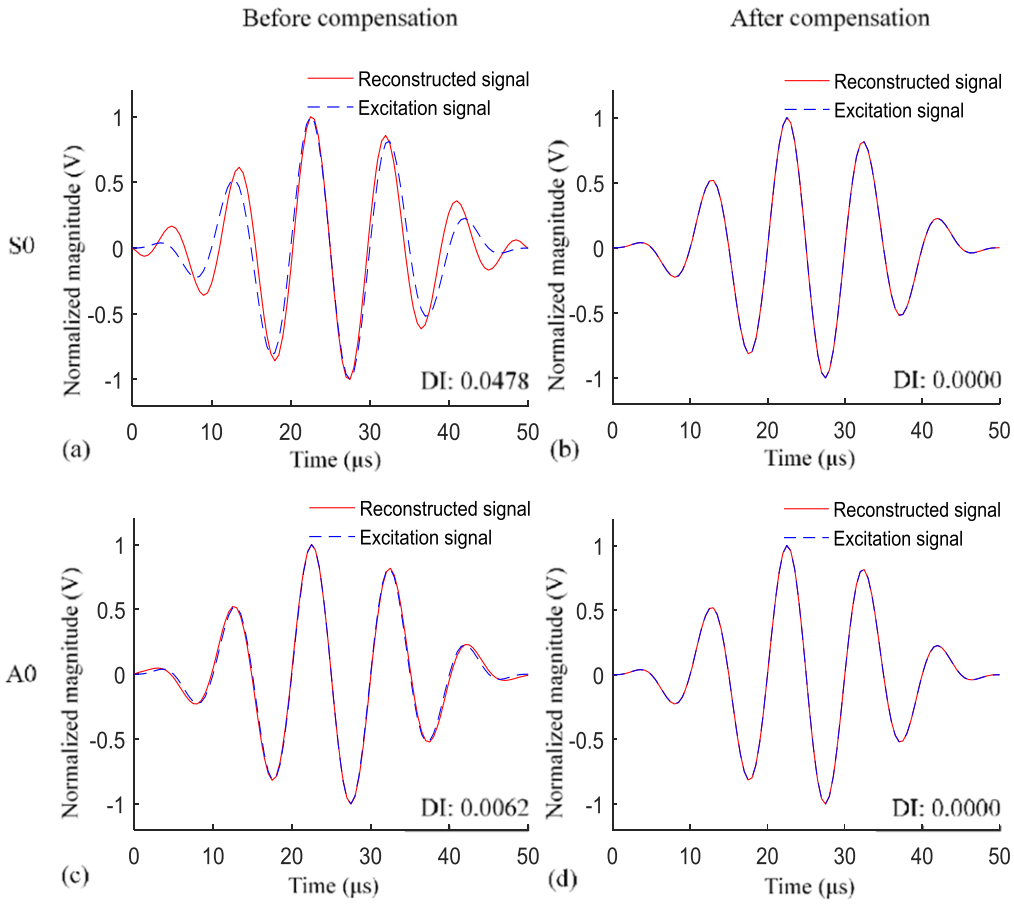

Figure 5. Virtual time reversal analytical results: (a) S0 mode before compensation; (b) S0 mode after compensation; (c) A0 mode before compensation; (d) A0 mode after compensation.

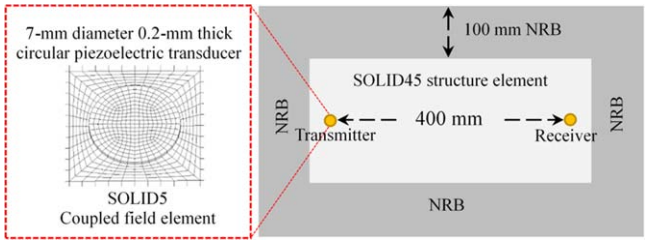

Figure 6. Finite element model for the pitch-catch procedure.

wire soldering and instrumentation, as well as curing. For details of the sensor implementation procedure, the readers are encouraged to explore page 379 of [39].

Damping clay was implemented surrounding the whole plate to absorbing the boundary reflections. A Keysight 33500B arbitrary function generator was used to generate excitation waveforms. The excitation signal was further amplified by a Krohn-hite 7602M wideband power amplifier and applied on the transmitter. Guided waves were generated by the piezoelectric transducer, propagating along the plate and were finally picked up by the receiver PWAS. The sensing waveforms were collected by the Keysight DSO-X 3014T digital storage oscilloscope. A 20 Vpp five-count Hanning window modulated sine tone burst signal centered at 100 kHz was applied on the electrode of the transmitter.

Figure 9 shows the VTR experimental results. Obvious reconstruction improvements can be noticed after the compensation procedure for both wave modes. Compared with previous analytical and FE simulation results, the deviation between the reconstructed signal and exaction waveform after compensation are greater. This is because inevitable errors may exist between analytical compensation function estimation and the practical transducer instrumentation. Individual sensor deviations, installation operations, and bonding layer involvement may all contribute to such errors. However, the overall tendency and improvement over the conventional VTR results correspond well to the previous investigation results.

5. Breakage of time reversibility in the presence of damage

In order to demonstrate the breakage of time reversibility in the presence of damage, 2D finite element simulations are conducted. Figure 10 presents the schematics of both single S0 and A0 TR procedures. It should be noted that, only the damaged case is shown in figure 10, but the corresponding pristine case is also simulated for comparison. The mass block, bonded on the plate surface, serves as an ultrasonic wave scatterer, simulating a general structural damage. The

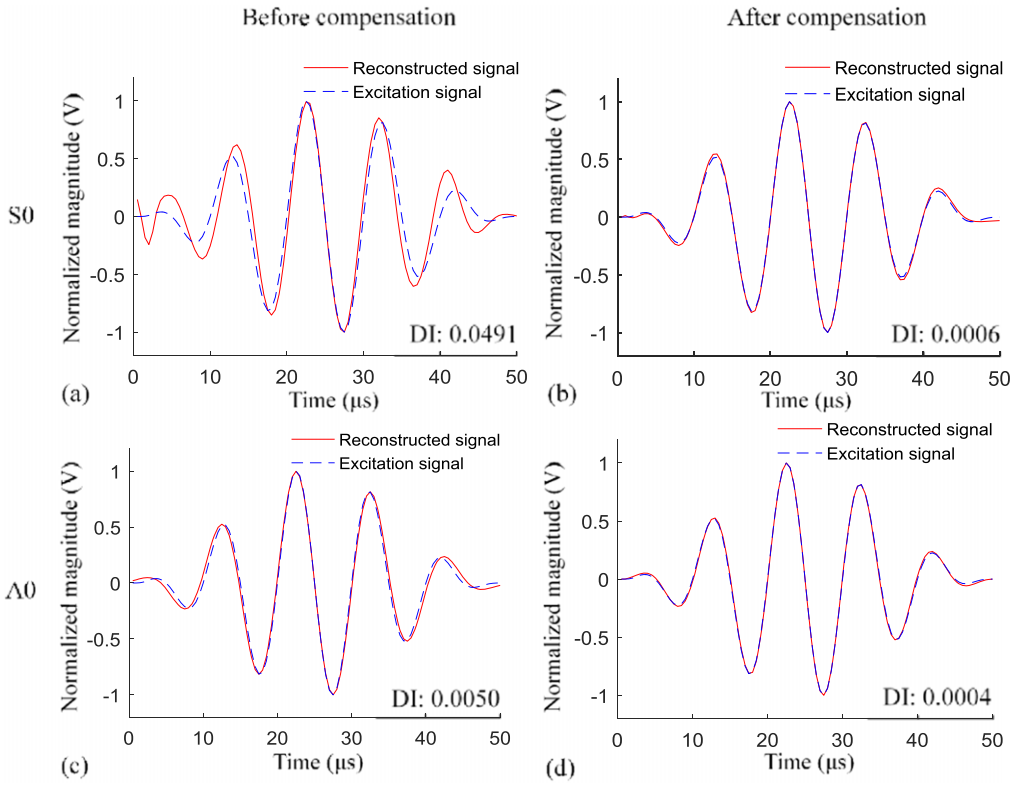

Figure 7. Virtual time reversal FE simulation results: (a) S0 mode before compensation; (b) S0 mode after compensation; (c) A0 mode before compensation; (d) A0 mode after compensation.

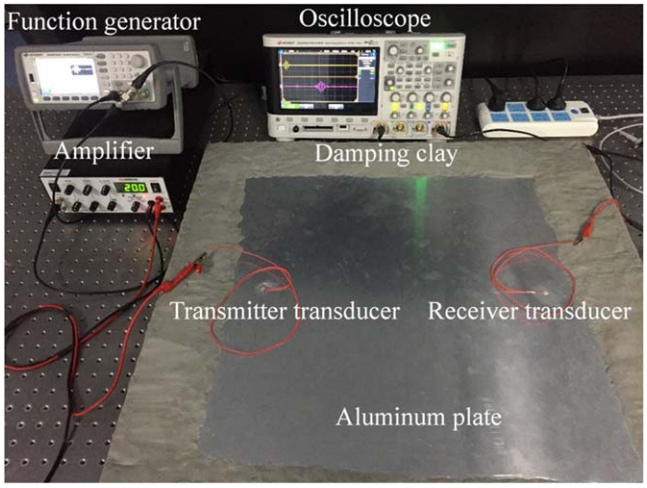

Figure 8. Experimental setup for pitch-catch active sensing.

structure is a 1 mm thick aluminum plate, and the length and thickness of the simulated damage are 20 mm and 2 mm, respectively. NRB are implemented at both ends of the plate to absorb boundary reflections. In figure 10, the red dots represent excitation points, exerting in-plane pin force oscillations; the blue dots stand for the sensing points, picking up in-plane strain components. In this way, pure wave mechanics is considered without any influence from transducers. ε stands for the nodal strain. In this case, only the strain component in the x direction is considered. A represents the amplification factor subjected to amplify the strain as the excitation force in the second reversing pitch-catch procedure. The superscripts T and B represent the top and bottom surfaces, respectively. And the subscripts 1 and 2 stand for the forward and backward pitch-catch procedures, respectively. In addition, the excitation force is a five-count Hanning window modulated sine tone burst signal centered at 200 kHz.

The benefit of utilizing finite element simulation for such a demonstration resides in the fact that ideal single mode TR procedure can be achieved. For the S0 mode case, the first forward propagation procedure applies the equal-magnitude, in-phase pin force oscillations on both top and bottom surfaces, which allows the generation of single S0 mode interrogating wave field into the structure. This S0 wave propagates along the structure, interacts with the scatterer, takes the damage signature with it, undertakes transmission, reflection, mode conversion, and finally arrives at the sensing location. Then, the nodal in-plane strain on top and bottom surfaces at the sensing location is recorded. The S0 mode component arriving at the sensing location is extracted by the summation of the strain components on both top and bottom surfaces, divided by a factor of 2. Next, the backward propagation pitch-catch procedure is realized by applying the time reversed sensing signals as pin force excitations at the new wave generation points (the original sensing location in the forward procedure). The final reconstructed signal is recovered using the average strain in the backward pitch-catch procedure at the new sensing location (the original excitation location in the forward procedure). In this manner, time reversed single S0 mode can be obtained, although mode converted A0 waves do exist in the wave field. For the A0

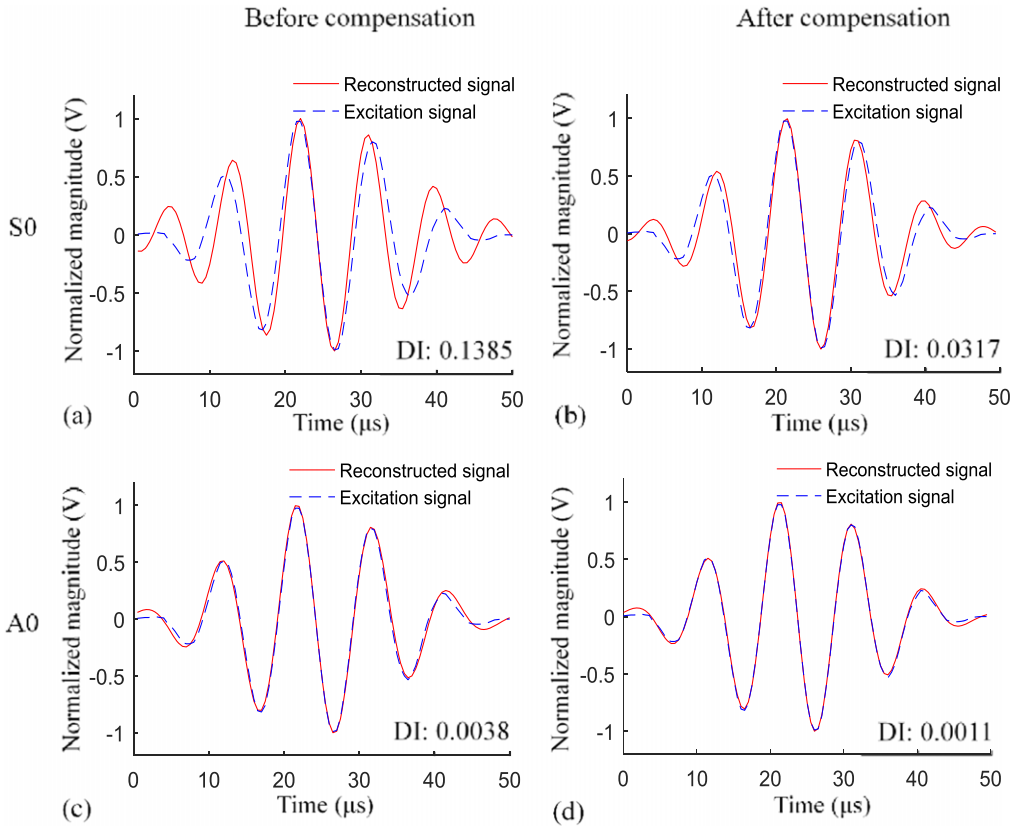

Figure 9. Virtual time reversal experimental results: (a) S0 mode before compensation; (b) S0 mode after compensation; (c) A0 mode before compensation; (d) A0 mode after compensation.

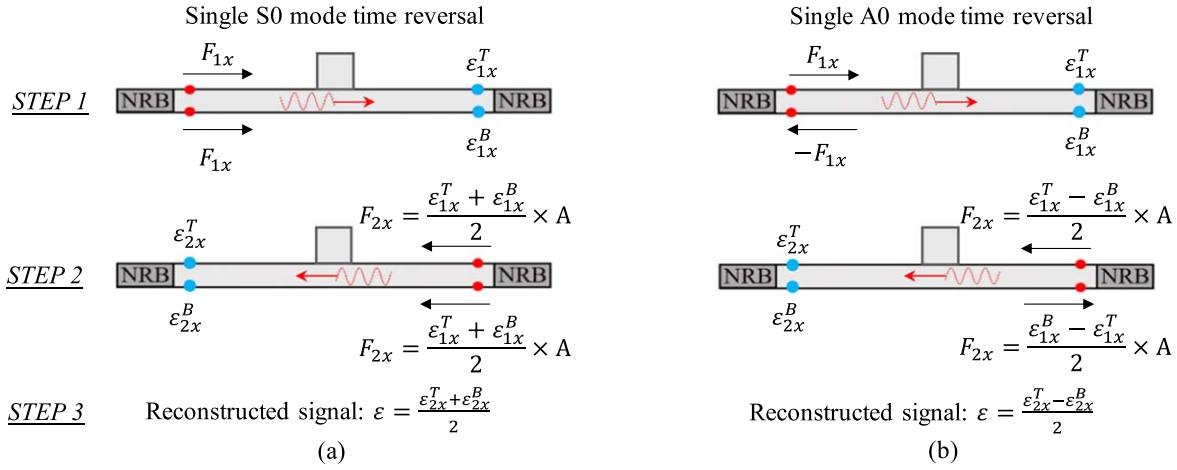

Figure 10. Schematics of breakage of time reversibility investigation considering both single S0 and A0 wave modes: (a) single S0 mode time reversal; (b) single A0 mode time reversal.

mode case, the procedure is similar; the only difference is that the pin forces are anti-phase on top and bottom surfaces for wave generation; the mode extraction from strain components utilizes the subtraction between the top and bottom sensing quantities, divided by a factor of 2.

Figure 11 shows the reconstructed signals of single S0 and A0 TR procedure. For the pristine case, the reconstructed signals match remarkably well with the excitation waveform for both S0 and A0 modes. And the DI values indicate the nice time reversibility of both wave modes. However, the presence of structural damage breaks the time reversibility, since the reconstructed signals in figures 11(c) and (d) apparently deviate from the excitation waveform. In addition, the DI values increase noticeably after introducing the scatterer. Thus, these results clearly demonstrate that the time reversibility is broken in the presence of damage. Furthermore, the reconstructed A0 mode deviates much more than S0 mode from the excitation signal, which means A0 mode is more sensitive to such type and dimension of structural damage. In other words, the sensitivity of various wave

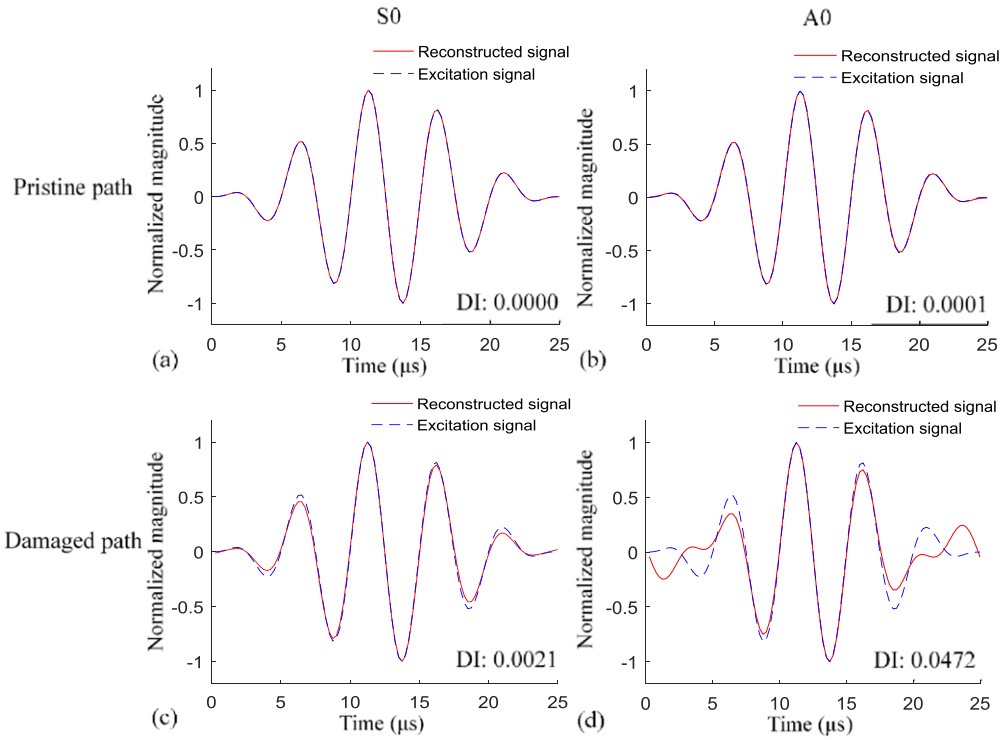

Figure 11. Reconstructed signals of single S0 and A0 time reversal procedure: (a) S0 mode on pristine path; (b) A0 mode on pristine path; (c) S0 mode on damaged path; (d) A0 mode on damaged path.

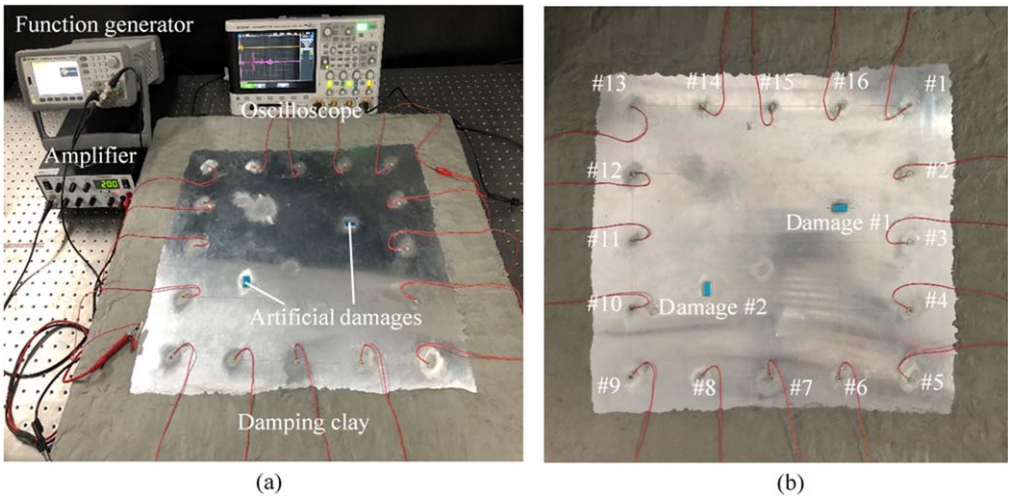

Figure 12. VTR damage imaging tests: (a) experimental setup; (b) specimen with a square active sensing PWAS array.

modes at different frequencies with distinct wavelengths and motion characteristics to diverse types of damage scenarios may differ much from case to case (notch, delamination, fatigue crack, etc). The selection of sensitive wave modes and frequency to detect a certain type of damage is a classical topic and complex task and should be investigated in another comprehensive study.

6. Enhanced damage imaging via VTR tomography

To demonstrate and validate the advantage of the proposed transducer transfer function compensation operation, conventional and enhanced VTR algorithms were performed on the same experimental setup. An active sensing array was designated to establish effective wave path coverage of the inspection area [40]. In this study, both S0 and A0 wave modes were employed for damage imaging as well as the fusion between their diagnostic information to strengthen the imaging quality.

6.1. Experimental setup

Figure 12 presents the experimental setup and the 1 mm thick aluminum plate for damage imaging. A total of 16 piezoelectric transducers were implemented, forming a square

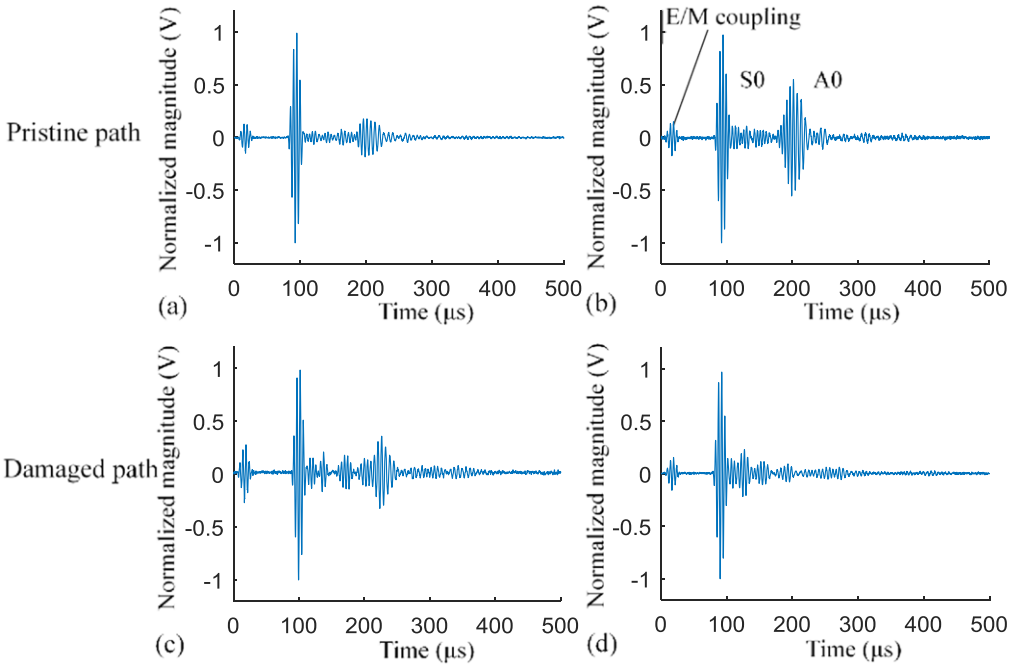

Figure 13. Experimental signals: (a) pristine path (#6-#15); (b) pristine path (#16-#7); (c) damaged path (#2-#10); (d) damaged path (#16-#6).

shape. The distance between the neighboring transducers was 100 mm. Two rectangular aluminum blocks were bonded on the plate as scatterers to mimic structural damage sites. The dimensions of scatterers are 20 mm long, 10 mm wide, and 2 mm thick.

In this active sensing array, each transducer can serve as both a transmitter and a receiver. A 20 Vpp five-count Hanning window modulated sine tone burst signal centered at 200 kHz was applied on the electrode of each piezoelectric transducer. Such an excitation frequency rendered comparable wavelength to the scatterers dimensions, so as to offer sensitive diagnostic information. For each transmitter, the corresponding farthest seven transducers would serve as sensors. The sensing array operated in a Round-Robin fashion. Therefore, a total number of 112 pitch-catch wave paths were involved, achieving effective coverage of the inspection area.

6.2. Example signals

Two typical transducer paths, pristine and damaged, are chosen as examples for showcasing the efficacy of transducer transfer function compensation. Figure 13 presents the four experimental signals from the receiver along the pristine and damaged paths. In the very beginning of the temporal signals, the E/M coupling exists in all the sensing signals. Then, the S0 mode can be easily identified, followed by the signal features due to scattering and mode conversion from the transducers and the damage as well as the A0 wave package. It should be noted that the A0 mode in the damaged path differs much from that in the pristine path. Especially in figure 13(d), the A0 wave package pattern was obviously modified due to the presence of the damage, which further demonstrated the A0 mode was more sensitive to the damage at 200 kHz.

Figures 14 and 15 present the reconstructed signals for S0 and A0 modes, respectively. For the pristine path, after compensation, the reconstructed signal demonstrated much better time reversibility. In addition, the difference of reconstructed signal between the pristine and the damaged paths using enhanced VTR algorithm becomes greater than conventional VTR technique. For example, the DI of the reconstructed A0 mode for both pristine and damaged paths are over 0.2. However, after compensation, the DI of the reconstructed signal in the pristine path reduced to 0.0038, and the DI in the damaged path increased to 0.6137. Before compensation, both the transducer tuning effect and damage influence would contribute to the DI values. However, such a mixed contribution may establish in a constructive or a destructive manner, making it hard to distinct the damage influence. On the other hand, the compensation algorithm eliminates the tuning effect, highlighting the difference between the reconstructed signal and excitation signal due to the presence of damage. Thus, greater differentiability between the pristine and damaged paths has been achieved. Consequently, the enhanced VTR algorithm can significantly improve the damage imaging quality.

It should be noticed that the breakage of time reversibility is closely related to the damage types, damage characteristic details, the interrogating wave mode, the inspection frequency, and the incident angle. For example, Gangadharan *et al* demonstrated that time reversibility of Lamb waves could be maintained in the presence of a defect like a crack or a notch in the metallic plates [41]. In this study, added mass blocks bonded on the plate surface were used as a general scatterer to simulate the damage. The mechanism and rationale behind the breakage of time reversibility in our case resides in the fact that the dimension matching between the damage and the wavelengths

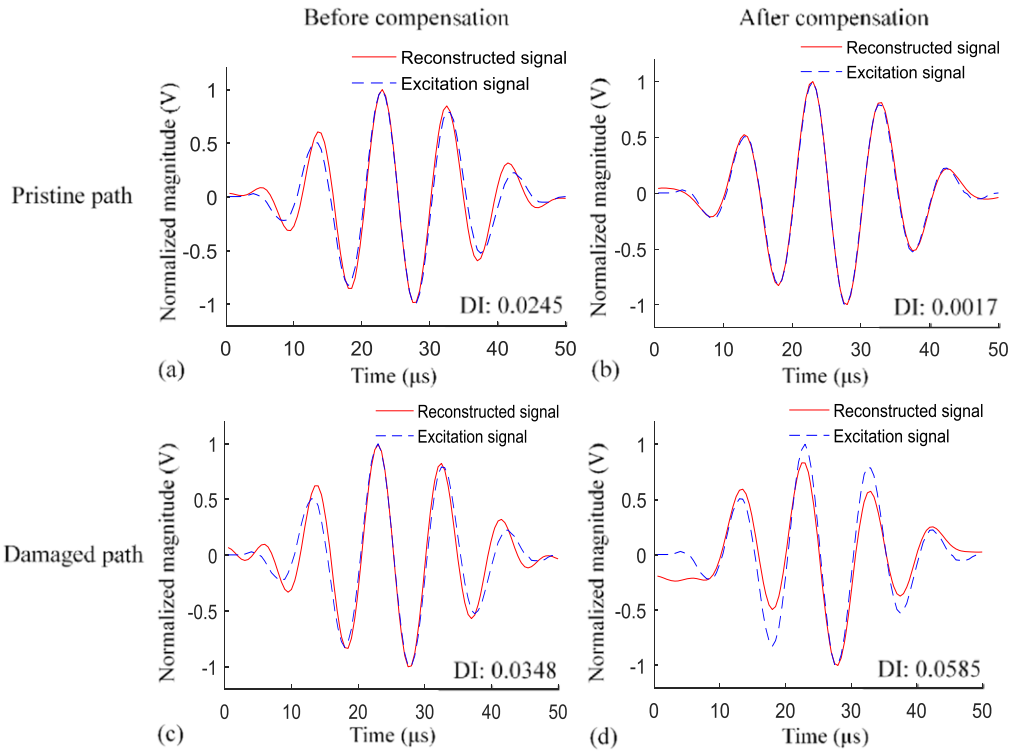

Figure 14. Reconstructed S0 signals: (a) pristine path before compensation (#6-#15); (b) pristine path after compensation (#6-#15); (c) damaged path before compensation (#2-#10); (d) damaged path after compensation (#2-#10).

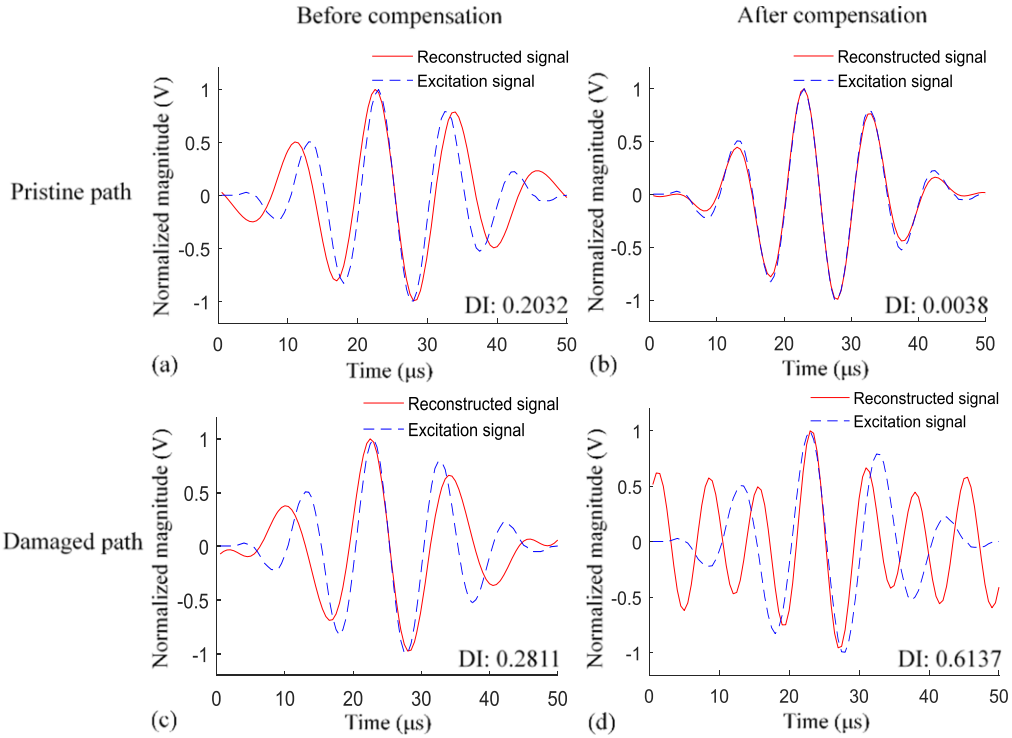

Figure 15. Reconstructed A0 signals: (a) pristine path before compensation (#16-#7); (b) pristine path after compensation (#16-#7); (c) damaged path before compensation (#16-#6); (d) damaged path after compensation (#16-#6).

would form local resonance at the damage, which would in turn modify the frequency component of the transmitted waves. The experimental results also correspond well with the previous finite element simulation which demonstrated the breakage of time reversibility in our case. Again, the sensitivity of the chosen wave mode, frequency, and incident angle towards the damage type and geometric characterizes matters in the active sensing procedures.

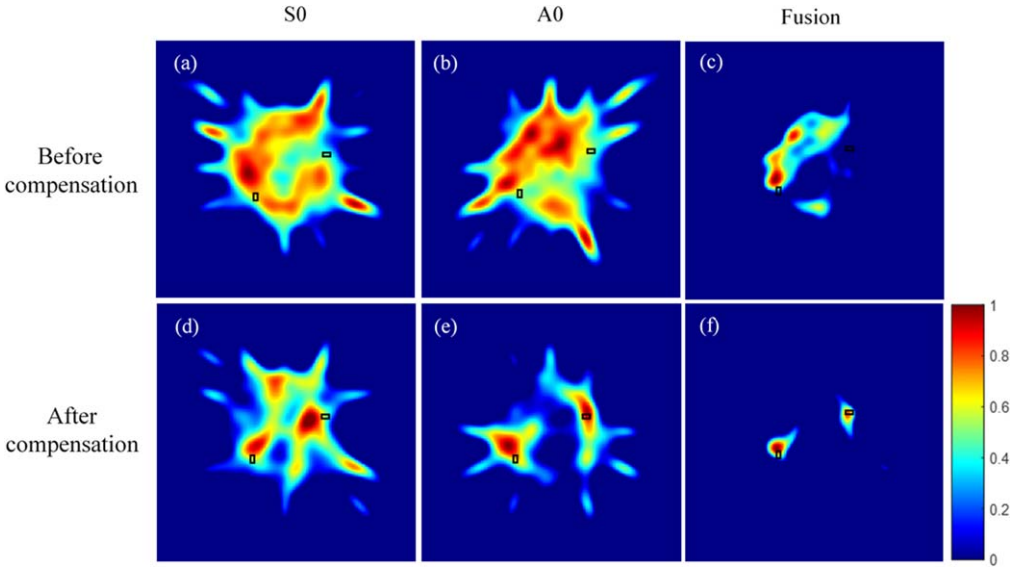

Figure 16. Damage imaging using the conventional VTR algorithm and the enhanced VTR algorithm: (a) S0 summation tomography before compensation; (b) A0 summation tomography before compensation; (c) fusion tomography before compensation; (d) S0 summation tomography after compensation; (e) A0 summation tomography after compensation; (f) fusion tomography after compensation.

6.3. Tomography damage imaging

The summation tomography algorithm was used for both S0 and A0 mode damage imaging. The probability of damage occurrence at position (x, y) at each direction produced by the path of each transmitter and receiver pair are added directly. The final VTR-based probabilistic imaging algorithm can be expressed as

$$P(x, y) = \sum_{m=1}^{M} \sum_{n=1}^{N} DI_{mn} E(R_{mn}(x, y)), \tag{18}$$

where $P(x, y)$ denotes the probability of damage occurrence at the position (x, y); M is the number of transmitters; N represents the number of receivers for each transmitter; subscript mn indicates the nth receiver of the mth transmitter, $R_{mn}(x, y)$ defines the distance between the position (x, y) and the Lamb wave ray excited by the corresponding transmitter; $E(R_{mn}(x, y))$ denotes the Gaussian function to estimate the energy distribution of Lamb wave ray, given by

$$E(R_{mn}(x, y)) = \begin{cases} \dfrac{1}{\sigma\sqrt{2\pi}} e^{-\left(\frac{R_{mn}(x,y)}{D}\right)^2 \Big/ 2\sigma^2} & R_{mn}(x, y) \leqslant D \\ 0 & R_{mn}(x, y) > D \end{cases}, \tag{19}$$

where D determines the width of Lamb wave ray excited by transmitter transducer and σ determines the decreasing ratio of Gaussian function. Herein, the parameters D and σ are respectively chosen as 32 mm and 0.32. The appropriate choice of these parameters would impose much influence on the image. Many previous investigations have been made for the scientific determination of these parameters. More details about imaging algorithm and the choice of imaging parameters can be found in [24].

Furthermore, the image fusion technique was adopted after [42]. The diagnostic images of both S0 and A0 modes are normalized and then processed with a point-by-point multiplication algorithm. Consequently, it incorporates the diagnostic information from both wave modes to achieve better localization and imaging of the damage sites.

Figure 16 presents the damage imaging comparison results between the conventional VTR and the enhanced VTR tomography algorithm. Before compensation, the damage sites cannot be located accurately via the S0 and A0 single mode summation tomography algorithm. The paths crossing the damage sites have not been highlighted. On the contrary, pristine paths present the high-pixel areas; one transducer area also possess high pixel values. In addition, there are some pseudo-focusing points, which apparently deviate from the true damage position. Although the imaging result can be improved after the fusion tomography algorithm, the first damage still cannot be imaged.

On the other hand, the damage imaging quality is apparently improved using the enhanced VTR tomography algorithm with transducer transfer function compensation. There are obviously two high-pixel areas in the single mode images, representing two damage sites respectively. Pristine and damaged paths can be clearly identified, showing the probability of the interrogating Lamb wave passing the damage sites. Although the imaged damage position deviates a little bit from the true damage sites, it has been obviously improved using the fusion tomography algorithm. The damage sites can be accurately located via the fusion image.

The in-plane dimensions of the damage are 20 mm × 10 mm. The wavelength of S0 mode is 27 mm, longer than the dimensions of damage. So, S0 mode is not so sensitive to the damage. On the other hand, A0 mode possesses a wavelength of 7 mm, much smaller than the damage dimensions, indicating a much stronger interaction between A0 waves and the damage. Hence, after compensation, all the paths present lower DI values for S0 mode compared with A0 mode. Consequently, pristine and damaged paths cannot be well differentiated for S0 mode tomography images; a spurious damage location appears in the S0 summation

tomography algorithm. On the other hand, the A0 mode is more sensitive to the damage; A0 mode renders much better imaging results than S0 mode.

7. Concluding remarks and future work

This article presented an enhanced Lamb wave VTR algorithm with transducer transfer function compensation. In the conventional VTR method, the transducer tuning effect modifies the frequency components. As a result, the reconstructed signal could not agree well with the excitation waveform. When it comes to damaged cases, it is hard to tell whether the breakdown of time-reversibility is associated with the presence of damage or the transducer participation.

Our investigation started with the analytical formulation for the identification of transducer transfer functions. The theoretical basis and computerized procedure for the enhanced VTR algorithm was subsequently introduced. Case study examples using the analytical solution, finite element simulations, and experiments were presented. It was found that the reconstructed signals after compensation achieved much better time reversibility than those without the compensation. In particular, the reconstructed signals attained from the analytical solution realized the complete reconstruction of the excitation waveform. Finally, a damage imaging experiment was performed to validate the efficacy of transducer transfer function compensation algorithm. The imaging results were considerably improved using the enhanced VTR technique. And the image fusion combining both S0 and A0 mode tomography results showed remarkable diagnostic accuracy.

For future work, the enhanced VTR algorithm should be attempted for detecting damage in the anisotropic composite plates. The nonlinear TR algorithm should be investigated for detecting fatigue cracks.

Acknowledgments

The support from the National Natural Science Foundation of China (contract number 51605284) is thankfully acknowledged.

ORCID iDs

Yanfeng Shen https://orcid.org/0000-0002-3025-4664

References

[1] Yu L Y and Giurgiutiu V 2006 Design, implementation, and comparison of guided wave phased arrays using embedded piezoelectric wafer active sensors for structural health monitoring *Proc. SPIE* **6173** 61731M
[2] Giurgiutiu V, Yu L, Kendall J R and Jenkins C 2007 *In-situ* imaging of crack growth with piezoelectric-wafer active sensors *AIAA J.* **45** 2758–69
[3] Ahmad R, Kundu T and Placko D 2005 Modeling of phased array transducers *J. Acoust. Soc. Am.* **117** 1762–76
[4] Yu L, Bottai-Santoni G and Giurgiutiu V 2010 Shear lag solution for tuning ultrasonic piezoelectric wafer active sensors with applications to Lamb wave array imaging *Int. J. Eng. Sci.* **48** 848–61
[5] Zhou C, Hong M, Su Z, Wang Q and Cheng L 2013 Evaluation of fatigue cracks using nonlinearities of acousto-ultrasonic waves acquired by an active sensor network *Smart Mater. Struct.* **22** 015018
[6] Shen Y and Giurgiutiu V 2013 Predictive modeling of nonlinear wave propagation for structural health monitoring with piezoelectric wafer active sensors *J. Intell. Mater. Syst. Struct.* **25** 506–20
[7] Srivastava A and di Scalea F 2009 On the existence of antisymmetric or symmetric Lamb waves at nonlinear higher harmonics *Proc. SPIE* **323** 932–43
[8] Wang C H, Rose J T and Chang F-K 2004 A synthetic time-reversal imaging method for structural health monitoring *Smart Mater. Struct.* **13** 415–23
[9] Qiu L, Yuan S, Zhang X and Wang Y 2011 A time reversal focusing based impact imaging method and its evaluation on complex composite structures *Smart Mater. Struct.* **20** 105014
[10] Fink M 1992 Time reversal of ultrasonic fields: I. Basic principles *IEEE Trans. Ultrason. Ferroelectr. Freq. Control* **39** 555–66
[11] Ing R K and Fink M 1998 Time-reversed Lamb waves *IEEE Trans. Ultrason. Ferroelectr. Freq. Control* **45** 1032–43
[12] Qiang W and Shenfang Y 2009 Baseline-free imaging method based on new PZT sensor arrangements *J. Intell. Mater. Syst. Struct.* **20** 1663–73
[13] Wang J and Shen Y 2018 Numerical investigation of ultrasonic guided wave dynamics in piezoelectric composite plates for establishing structural self-sensing *J. Shanghai Jiaotong Univ. (Science)* **23** 175–81
[14] Park H W, Kim S B and Sohn H 2009 Understanding a time reversal process in Lamb wave propagation *Wave Motion* **46** 451–67
[15] Jeong H, Lee J S and Bae S M 2011 Imaging of a defect in thin plates using the time reversal of single mode lamb wave: simulation *J. Korean Soc. Nondestructive Testing* **1330** 1523–30
[16] Qu W, Xiao L, Zhou Y and Inman D J 2013 Lamb wave damage detection using time reversal DORT method *Smart Mater. Struct.* **22** 045014
[17] Poddar B, Kumar A, Mitra M and Mujumdar P M 2011 Time reversibility of a Lamb wave for damage detection in a metallic plate *Smart Mater. Struct.* **20** 025001
[18] Gangadharan R, Murthy C R, Gopalakrishnan S and Bhat M R 2011 Time reversal health monitoring of composite plates using Lamb waves *Int. J. Aerosp. Innov.* **3** 131–42
[19] Normandin B and Veidt M 2013 Single transducer pair Lamb wave time reversal for damage detection in composite laminates *Key Eng. Mater.* **558** 205–17
[20] Sohn P H W *et al* 2007 Damage detection in composite plates by using an enhanced time reversal method *J. Aerosp. Eng.* **20** 141–51
[21] Agrahari J K and Kapuria S 2015 A refined Lamb wave time-reversal method with enhanced sensitivity for damage detection in isotropic plates *J. Intell. Mater. Syst. Struct.* **27** 1283–305
[22] Watkins R and Jha R 2012 A modified time reversal method for Lamb wave based diagnostics of composite structures *Mech. Syst. Signal Process.* **31** 345–54
[23] Zeng L, Lin J and Huang L 2017 A modified Lamb wave time-reversal method for health monitoring of composite structures *Sensors* **17** 955–969

[24] Liu Z, Yu H, Fan J, Hu Y, He C and Wu B 2015 Baseline-free delamination inspection in composite plates by synthesizing non-contact air-coupled Lamb wave scan method and virtual time reversal algorithm *Smart Mater. Struct.* **24** 045014
[25] Cai J, Shi L, Yuan S and Shao Z 2011 High spatial resolution imaging for structural health monitoring based on virtual time reversal *Smart Mater. Struct.* **20** 055018
[26] Kim D K, Lee J K, Seung H M, Park C I and Kim Y Y 2018 Omnidirectional shear horizontal wave based tomography for damage detection in a metallic plate with the compensation for the transfer functions of transducer *Ultrasonics* **88** 72–83
[27] Giurgiutiu V 2016 Tuned Lamb wave excitation and detection with piezoelectric wafer active sensors for structural health monitoring *J. Intell. Mater. Syst. Struct.* **16** 291–305
[28] Yu L and Giurgiutiu V 2008 *In situ* 2D piezoelectric wafer active sensors arrays for guided wave damage detection *Ultrasonics* **48** 117–34
[29] Xu B and Giurgiutiu V 2007 Single mode tuning effects on Lamb wave time reversal with piezoelectric wafer active sensors for structural health monitoring *J. Nondestruct. Eval.* **26** 123–34
[30] Shen Y and Giurgiutiu V 2014 WaveFormRevealer: an analytical framework and predictive tool for the simulation of multi-modal guided wave propagation and interaction with damage *Struct. Health Monit.: Int. J.* **13** 491–511
[31] Lin B and Giurgiutiu V 2011 Power and energy transduction analysis of piezoelectric wafer-active sensors for structural health monitoring *Struct. Health Monit.: Int. J.* **11** 109–21
[32] Shen Y and Giurgiutiu V 2016 Combined analytical FEM approach for efficient simulation of Lamb wave damage detection *Ultrasonics* **69** 116–28
[33] Yeum C M, Sohn H and Ihn J B 2011 Lamb wave mode decomposition using concentric ring and circular piezoelectric transducers *Wave Motion* **48** 358–70
[34] Raghavan A and Cesnik C E S 2005 Finite-dimensional piezoelectric transducer modeling for guided wave based structural health monitoring *Smart Mater. Struct.* **14** 1448–61
[35] Graff K F 1991 *Wave Motion in Elastic Solids* (New York: Dover)
[36] Rose J L 1999 *Ultrasonic Waves in Solid Media* (Cambridge: Cambridge University Press)
[37] Lin B, Kamal A, Giurgiutiu V and Kamas T 2012 Multimodal Lamb waves power and transfer function analysis of structurally-bonded PWAS *Proc. ASME Conf. on Smart Materials, Adaptive Structures and Intelligent Systems (Sone Mountain, Georgia, USA)* (in English)
[38] Velichko A and Wilcox P D 2012 Efficient finite element modeling of elastodynamic scattering with non-reflecting boundary conditions *Review of Progress in Quantitative Nondestructive Evaluation* (https://doi.org/10.1063/1.4716224)
[39] Giurgiutiu V 2014 Piezoelectric wafer active sensors—PWAS transducers *Structural Health Monitoring with Piezoelectric Wafer Active Sensors* Second edition (Oxford, UK: Elsevier Academic Press) pp 357–94
[40] Zhao X, Royer R L, Owens S E and Rose J L 2011 Ultrasonic Lamb wave tomography in structural health monitoring *Smart Mater. Struct.* **20** 105002
[41] Gangadharan R, Murthy C R, Gopalakrishnan S and Bhat M R 2009 Time reversal technique for health monitoring of metallic structure using Lamb waves *Ultrasonics* **49** 696–705
[42] Michaels J E and Michaels T E 2007 Guided wave signal processing and image fusion for *in situ* damage localization in plates *Wave Motion* **44** 482–92